Materials Advances

ROYAL SOCIETY OF CHEMISTRY

PAPER

View Article Online
View Journal | View Issue

Cite this: *Mater. Adv.*, 2025, **6**, 4680

Accelerated perovskite discovery: screening new catalysts for photocatalytic methylene blue degradation†

Poulami Mukherjee,* Yohei Cho, Phulkerd Panitha and Toshiaki Taniike*

Received 10th April 2025,
Accepted 27th May 2025

DOI: 10.1039/d5ma00345h

rsc.li/materials-advances

The diversified use of metal oxides within several disciplines underlines their flexibility in various catalytic processes and innovations in materials science. Due to their tailored functionality, improved stability, and enhanced conductivity, multimetallic oxides offer a wider range of applications compared to single-metal counterparts. Among them, perovskites stand out, being a class suitable for various applications, including photocatalysis. One among them is the photocatalytic degradation of methylene blue (MB), a process increasingly recognized for its importance in environmental remediation and water purification. Herein, we present a simple, economical, and easily adaptable high-throughput experimental approach to synthesize and evaluate a wide array of citric acid-assisted perovskite compositions for photocatalytic degradation. Our high-throughput approach not only addresses the bottleneck of catalyst preparation but also expands the scope of photocatalysis research by incorporating computational screening of less-explored perovskite compositions. The obtained data will serve as a valuable reference for the development of next-generation catalysts, as we have drawn a correlation between material properties and their performance. Moreover, the synthetic methodology, if adopted, enables the synthesis of any kind of metal oxides for applications ranging from homogeneous and heterogeneous catalysis to broader domains of materials science.

1. Introduction

Robust-performance metal oxides represent one of the most versatile classes of materials in modern science, owing to the possibilities of tailoring their structural, electronic, and chemical properties in ways that make them critical in various fields ranging from environmental catalysis to energy conversion and storage.[1–3] Having the feasibility of leveraging additional metals with varying properties, multi-metal oxides offer a wider range of functions with improved performance, stability, and enhanced conductivity compared to single-metal-based oxides.[4,5] Among them, perovskites represent a special class of metal oxides, which are particularly striking due to their adaptability, and find vital applications across various scientific disciplines.[2,5,6]

Amidst the major applications of perovskite materials, photocatalysis has a greater drive toward improving energy efficiency in chemical reactions in a sustainable manner.[7–10] The degradation of the environmental pollutant methylene blue (MB), a common cationic dye used in many industries, has been one of the main areas of focus in photocatalysis.[11,12] MB is a non-biodegradable compound and has become an important environmental pollutant, especially in water ecosystems.[13] The increasing application of the compound has necessitated the development of effective and sustainable methods for its removal from wastewater.[14,15] Conventional methods such as adsorption,[16,17] coagulation,[18] and biological treatments[19] often lead to incomplete degradation, accompanied by drawbacks such as high operational costs and the generation of secondary pollutants. In this aspect, advanced oxidation processes are especially appealing because, using sunlight as an activator of photocatalysts, they allow organic dyes to be completely mineralized into environmentally benign end products such as CO_2 and H_2O.[20–24]

Perovskite materials have a unique ability to incorporate a wide range of elements and provide enhanced tunability of band positions, charge carrier mobility, and other electronic properties.[2,7] Such wide composition flexibility in the case of an ABO_3 perovskite structure is enabled by the possibility of varying both A- and B-site cations within a tolerance factor of approximately 0.8–1.0.[25] In fact, it is certain that each variation can significantly impact the photocatalytic efficiency of the material. Thus, systematic screening of a large number of material compositions under various conditions is essential to exploring

Graduate School of Advanced Science and Technology, Japan Advanced Institute of Science and Technology, 1-1 Asahidai, Nomi, Ishikawa, 923-1292, Japan.
E-mail: poulami1396@gmail.com, taniike@jaist.ac.jp

† Electronic supplementary information (ESI) available. See DOI: https://doi.org/10.1039/d5ma00345h

a vast parameter space efficiently and identifying optimal combinations that maximize MB degradation. In this prospect, making the synthesis and evaluation at comparable throughput is of utmost importance. By scaling up materials exploration, new high-performance materials that might not have been explored by conventional trial-and-error approaches could be discovered, thereby advancing the development of more effective and sustainable photocatalytic solutions. To achieve this, an approach mandating high-throughput experimentation (HTE) in both catalyst preparation and performance evaluation will be required.[26–29] While the term HTE may initially sound a little overwhelming for materials researchers, complexity in synthesis and evaluation processes is inevitable because humans lack efficiency in managing and analyzing a huge array of variables that cover material compositions, processing conditions, and performance metrics. Needless to say, the real bottleneck in such catalysis research lies in the labor-intensive preparation methods for the catalysts.

Among the different synthesis methodologies, the citric acid-assisted synthesis of metal oxides, including perovskites, has several notable advantages compared to the conventionally used techniques such as combustion, solid-state reactions, hydrothermal synthesis, co-precipitation, and classical sol–gel processes.[30,31] In metal oxide synthesis, citric acid (CA), as a complexing agent, can stabilize the metal ions, preventing their premature precipitation. It also accelerates gelation, promoting the formation of a homogeneous precursor gel.[32,33] The two characteristics are very important in the case of ternary or quaternary metal oxide formation, where the CA matrix inhibits the phase segregation during the synthesis, ensuring a single-phase product without impurities. Typically, ionic nitrate salts are preferred in this process since they typically tend to be stronger oxidizers compared to pure oxygen. Together with organic citrate salts, they undergo a low-temperature oxidation–reduction reaction and self-ignite. Finally, the process is relatively simple and can be easily scaled up for industrial applications.

In light of all these merits, this study tackles the challenges of HTE by designing a parallelizable synthetic route for CA-assisted perovskite materials and screening their photocatalytic activity for MB degradation. The study highlights the role of CA in perovskite synthesis by comparing selected samples prepared with and without CA. By analyzing the morphological differences between these samples, we demonstrate how CA influences principal synthesis parameters like nucleation and particle dispersion and acts as a structure-directing agent to form either well-dispersed nanoparticles or an ordered framework, depending on the elemental composition. Besides the perovskite synthesis for MB degradation, the wide applicability of high-throughput synthesis approaches extends to synthesizing any mixed oxides that might find applications in catalysis, energy storage, sensors, and environmental protection, among many others. The scope of the study includes perovskites that are not commonly studied for photocatalysis, yet show potential for effective MB degradation, as filtered by using a computational database based on several key factors. The results obtained from this study will guide the readers not only to parallelizable synthetic techniques, which allow rapid synthesis of many catalysts within a short time frame, but also to the fact that the photocatalytic screening results were obtained under unified conditions will allow researchers to observe trends, correlations, and design principles for future materials exploration using the synthesized perovskites as valuable reference data. The potential impact of multiple physical properties on photocatalytic performance was estimated through statistical analysis.

2. Experimental method

2.1. Materials selection

17 materials were selected for the photocatalytic degradation of MB from the Materials Project database[34,35] for photocatalytic degradation of MB based on the following criteria:

1. The material includes the original selection of 23 elements. Elements whose oxides are widely employed in heterogeneous reactions, especially redox catalysis, are focused. Certain elements, namely molybdenum (Mo) and chromium (Cr), are intentionally excluded due to sublimation risks and safety issues. Table S1 (ESI†) lists the chosen elements with their precursor salts.

2. Energy_above_hull (parameters relating to stability) = 0, and the materials are listed in the ICSD. The energy above the hull measures the thermodynamic stability of a given material.[34] If the energy value is 0 eV, it means that the material lies on the convex hull of stability, which, physically, means that it will not spontaneously decompose into other phases since this is the most stable phase. This is a critical parameter in the first-level screening of a material's synthesizability, with the consideration that photocatalysts must withstand the conditions of the reaction without degrading or being converted into less active phases. To further ensure synthesizability, those combinations that are listed in the Inorganic Crystal Structure Database (ICSD) are preferred, allowing us to claim success for our high-throughput synthesis method.

3. The chemical formula is represented in the ABO_3 form, where A and B are elements selected based on criterion 1, and O corresponds to oxygen. For the broad applicability of perovskite materials, the synthesis of perovskite structures is intended by a parallel approach.

4. Bandgap within the range of 0.5–4.0 eV. A bandgap in this range is necessary for both absorbing sufficient sunlight to generate electron–hole pairs and having the overpotential required to drive photocatalytic reactions. A too small bandgap is inappropriate as it does not satisfy the thermodynamic criteria for conduction/valence band edge positions higher/lower than the redox potential, respectively, and cannot drive photocatalytic reactions. Conversely, a bandgap that is too large cannot absorb optimal sunlight to generate an electron–hole pair and will not drive the reaction. It should be noted that the calculated bandgap is usually underestimated compared to the experimentally obtained value, but to cover the large variety, a wider range than that of sunlight is set.

Table S2 (ESI†) displays the list of the 17 candidates chosen for perovskite synthesis.

2.2. High-throughput synthesis of perovskite materials

Here, the synthesis procedure of 17 perovskites is demonstrated. At first, 16 precursor solutions were prepared by dissolving individual metal nitrate salts in 20 mL of deionized (DI) water. The solutions were stirred with a multi-stirrer for 30 minutes to ensure homogeneity. Next, 20 mL of CA was added to each of the 16 solutions in a metal : CA molar ratio of 0.5 : 1.0 and stirred at 60 °C for an additional 30 minutes to prepare the stock solutions. The solutions thus formed were stored in a refrigerator.

It is important to note that titanium tetrabutoxide [$Ti(OCH_2CH_2CH_2CH_3)_4$] was used as the titanium precursor, which was freshly prepared by dissolving it in absolute ethanol. Additionally, the CA solution was also prepared in absolute ethanol. Both preparation processes were conducted under an inert atmosphere to prevent side reactions. All other conditions were consistently maintained, as previously described.

To prepare the final reaction solutions, 10 mL of the desired individual metal stock solution was added to reach a total volume of 20 mL for each mixture (Fig. 1(a)). These solutions were then evaporated at 100 °C under continuous stirring conditions (Fig. 1(b)). After 4–5 hours, the formed gels (Fig. 1(c)) were transferred to crucibles while still warm and less viscous. They were then dried in a muffle furnace at 120 °C for 12 hours. The semi-solidified gels were crushed to break any foaming caused during the degassing process. The crushed products obtained were subsequently calcined in a muffle furnace, first at 350 °C and then at 1000 °C, with a controlled heating rate of 2 °C per minute (Fig. 1(d)). Afterward, the final products were milled to produce fine perovskite powders (Fig. 1(e)). To investigate the role of CA in metal oxide synthesis, a few metal oxides, namely $CaTiO_3$, $SrTiO_3$, $MgTiO_3$, and $CaZrO_3$, were also prepared without CA, following the same procedure, except for the addition of CA. These perovskites were specifically selected due to their variation in their photocatalytic performance and compositional similarity in the included cations: Among the perovskites with titanium on B-site, $CaTiO_3$ was selected for its particularly high activity, $MgTiO_3$ for its notably low performance, and $SrTiO_3$ for its intermediate activity and extensive coverage in prior studies. $CaZrO_3$ which shares Ca with $CaTiO_3$ and contains Zr, which belongs to the same group as Ti and lies one period below it, was also chosen.

2.3. Materials characterization

The XRD patterns were recorded in the 2θ range of 3–90° at a scanning rate of 10° min^{-1} and a step size of 0.01° using a MiniFlexC600 (Rigaku) with Cu Kα radiation (λ = 1.5418 Å). The morphologies of the as-synthesized perovskites were examined by TEM using an H-7650 (Hitachi, Tokyo, Japan) at an acceleration voltage of 100 kV. The samples were dispersed in ethanol *via* ultrasonication for 15 min, then dropped onto a carbon-coated copper grid and naturally dried overnight. N_2 adsorption/desorption experiments were performed on a BELSORP Mini (BEL Japan, Tokyo, Japan) instrument at 77 K. An amount of 80–100 mg of the catalyst was loaded into a glass cell, followed by degassing under vacuum at 150 °C for 2 h before the measurement.

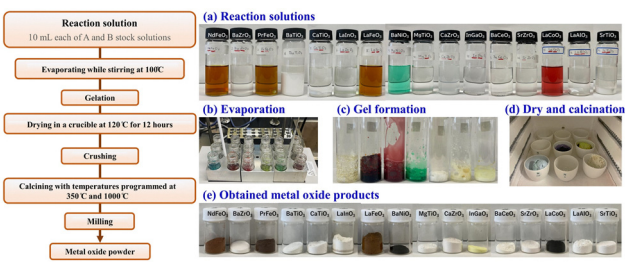

Fig. 1 Schematic illustration of the catalyst synthesis process.

2.4. High-throughput photocatalyst screening

A xenon (Xe) lamp with a light spectrum proximate to sunlight was employed, delivering an intensity of 250 W m^{-2}. The reaction was carried out under practical conditions at 20 °C. The MB concentration was fixed at 6.6 ppm to ensure adequate sensitivity for its detection. 100 μg of each perovskite sample included in Table 1 was used in the reaction. After adsorption for 1 h, we monitored the samples in the dark for another hour to evaluate their dark performance. Then, the samples were exposed to light for 3 hours; the absorbance was measured every 15 minutes to monitor the degradation of MB. Each experiment was performed three times to ensure the reliability of the data (N = 3). The reaction was performed using a parallelized approach to efficiently manage the screening process. To evaluate the photocatalytic performance, the absorbance at the characteristic wavelength of 665 nm (OD_{665}) was monitored, while the background absorbance at 800 nm (OD_{800}) was simultaneously recorded. The effective absorbance was defined as $\Delta OD = OD_{665} - OD_{800}$. The reaction rate constant (k) was determined by performing a linear regression on the decay of ΔOD over time. The rate constant was then converted to account for the calibration coefficient (expressed in ppm per unit OD), the reaction volume, and the mass of the perovskite catalyst, according to eqn (1):

$$k = -\frac{d}{dt}(OD_{665} - OD_{800}) \times (\text{conversion coefficient}) \times \frac{\text{solution volume}}{\text{perovskite mass}}. \quad (1)$$

Table 1 Confirmation of product formation with their corresponding phases

No.	Combination	JCPDS No.	Crystal structure
1	$NdFeO_3$	00-025-1149	Monoclinic
2	$BaZrO_3$	00-006-0399	Cubic
3	$PrFeO_3$	00-019-1012	Orthorhombic
4	$BaTiO_3$	01-075-2116	Tetragonal
5	$CaTiO_3$	01-075-2100	Cubic
6	$LaInO_3$	00-008-0148	Undefined
7	Pr_2O_3, In_2O_3	00-047-1111, 01-088-2160	Hexagonal, cubic
8	$LaFeO_3$	00-015-0148	Orthorhombic
9	$BaNiO_3$	01-070-0108	Hexagonal
10	$MgTiO_3$	00-006-0494	Rhombohedral
11	$CaZrO_3$	00-035-0645	Orthogonal
12	$InGaO_3$	01-075-0975	Hexagonal
13	$BaCeO_3$	00-022-0074	Orthorhombic
14	$SrZrO_3$	01-074-2231	Cubic
15	$LaCoO_3$	00-048-0123	Rhombohedral
16	$LaAlO_3$	01-085-0848	Rhombohedral
17	$SrTiO_3$	01-074-1296	Cubic

3. Results and discussion

3.1. Characterization of the synthesized materials

Powder X-ray diffraction (PXRD) spectroscopy confirmed the successful synthesis of 16 perovskites. The diffraction patterns of each sample were matched with their corresponding Joint Committee on Powder Diffraction Standards (JCPDS) reference number (Table 1) to confirm the correct phase and crystallinity of the material. All the perovskites show well-developed diffraction peaks, suggesting a relatively large domain size. This is reasonable due to the high calcination temperature used in their synthesis. The XRD patterns of the 17 combinations are shown in Fig. S1 (ESI†).

It should be noted that in the efforts to synthesize 17 perovskites using the CA method, the successful synthesis of 16 perovskites was confirmed; the expected $PrInO_3$ was not formed. Instead, a mixed oxide phase consisting of Pr_2O_3 and In_2O_3 was observed. One possible reason for this unsuccessful synthesis may be that the reaction conditions, such as temperature and time, might not have been optimal for this ternary oxide. The reaction conditions may stabilize mixed oxides over the desired $PrInO_3$. Furthermore, it must be pointed out that while the CA-assisted synthetic route is reported to yield single-phase products, our screening of 17 metal oxides resulted in variability, meaning that phase purity depends on optimized conditions, as some XRD patterns contained small impurity peaks. However, by comparing the XRD patterns of powders synthesized with and without CA for $CaTiO_3$, $SrTiO_3$, $CaZrO_3$, and $MgTiO_3$ (Fig. S2(a)–(d), ESI†), it is unveiled that CA enhances the formation of the desired phase. Such an influence explained its ability to stabilize metal–citrate complexes, enable a homogeneous dispersion of cations, and suppress the formation of undesired phases.

Transmission electron microscopy (TEM) images further revealed the significant morphological differences induced by CA (Fig. 2). For $CaTiO_3$ and $SrTiO_3$, the samples prepared with CA display small, well-dispersed nanoparticles, confirming that CA is highly effective at inhibiting the agglomeration of particles and facilitating uniform dispersion (Fig. 2a and b, respectively). Without CA, however, there is significant agglomeration, resulting in large clusters of particles exposing less surface area (Fig. 2e and f, respectively). In $CaZrO_3$ and $MgTiO_3$, CA is ascribed to the formation of hexagonal-like, well-shaped particles with well-defined boundaries, indicative of controlled nucleation and growth with homogeneously sized particles (Fig. 2c and d, respectively). In the absence of CA, the materials exhibit more irregular and aggregated structures with ill-defined particle morphology (Fig. 2g and h, respectively). Thus, the influence of CA on the final morphology—whether forming well-dispersed nanoparticles or a well-organized structure—is largely governed by the elemental composition of the system. The choice of metal composition dictates how CA directs the nucleation, growth, and final organization of the material. Brunauer–Emmett–Teller (BET) surface area analysis further confirms that the impact of CA addition remains evident even after its complete removal through calcination at 1000 °C. The addition of CA during the synthesis increases the surface area of the perovskites due to improved particle dispersion and controlled growth with the chelating nature of CA, but the extent of CA influence varies with the elemental composition (Fig. 2i–l). The BET surface area and the pore volume of the four perovskites are summarized in Table S3 (ESI†).

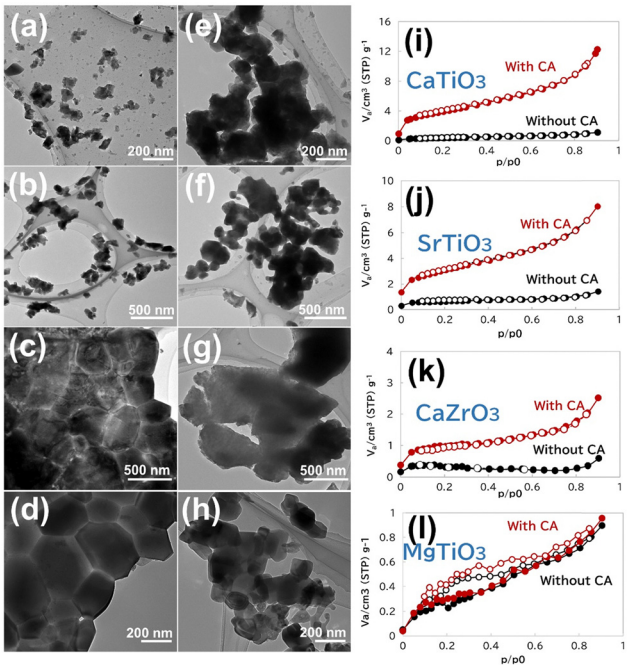

Fig. 2 TEM images of $CaTiO_3$, $SrTiO_3$, $CaZrO_3$, and $MgTiO_3$ synthesized with CA (a)–(d) and without CA (e)–(h), along with their corresponding N_2 adsorption–desorption isotherms (i)–(l).

3.2. Photocatalyst performance evaluation results

Fig. 3 illustrates the photocatalytic activities and the number of literature reports on 16 different ABO_3-type photocatalysts, along with a mixed oxide that did not become a single ABO_3-type structure. The raw decay data of MB and each material are shown

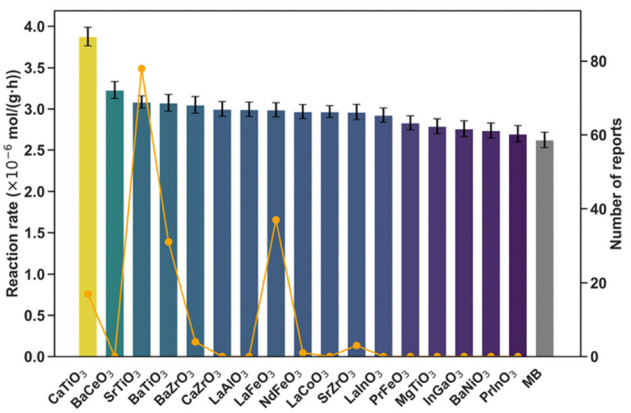

Fig. 3 Overlaid figures showing the photocatalytic performance and the number of reports for 16 ABO_3-type photocatalysts. The colored bars correspond to the reaction rate constants on the left axis, while the white line represents the number of reports on the right axis.

in Fig. S3 and S4 (ESI†). As shown in Fig. S5 (ESI†), compared to the light irradiation conditions, a negligible decrease is caused by either adsorption or dark performance within the 24-hour period. The perovskites are arranged in descending order with respect to their activities. The overlay in Fig. 3 also shows the number of previous reports on photocatalytic MB degradation for these perovskites, obtained through a Web of Science search conducted on August 28, 2024 using the keywords 'photocatalyst,' 'methylene blue,' and the respective perovskites' names.

In Fig. 3, all the samples are shown to catalyze MB decomposition more efficiently than photolysis. Among the samples, the reaction rates of $CaTiO_3$ and $BaCeO_3$ are notably higher than those of the other materials, including the most studied photocatalyst $SrTiO_3$. When comparing alkali earth metal–Ti-oxide photocatalysts, the observed trend follows $CaTiO_3 > SrTiO_3 \approx BaTiO_3 > MgTiO_3$, which mostly corresponds to their periods in the periodic table, except for $MgTiO_3$. Vijayakumar *et al.* reported that $MgTiO_3$ exhibited lower performance than $CaTiO_3$ in rhodamine B degradation.[36] They attributed this to the stronger Mg–O bonds in $MgTiO_3$, which make the bond cleavage and subsequent generation of reactive electron/hole pairs and radicals more difficult, while the weaker Ca–O bonds in $CaTiO_3$ facilitate these processes. Additionally, the aggregated nature of $MgTiO_3$ further reduced its photocatalytic activity. Similarly, various local factors govern photocatalytic performance. Investigating each of these factors in detail would be an extensive task beyond the scope of this study. However, while many efforts have been made to explore such individual local factors, this study aims to redefine a broader perspective by comparing a diverse range of materials under identical conditions.

A comparison between the performance ranking and the number of literature reports reveals that the high-performing materials identified in this study are not necessarily the ones most frequently investigated. Although it is generally expected that materials exhibiting superior performance would attract more research attention, discrepancies can possibly arise because previous studies often employ varied synthesis conditions (*e.g.*, temperature, atmosphere, methods, and the presence of optimized co-catalysts). Judging from the small number of publications, however, it is more probable that the materials have not been explored in sufficient depth. In practice, many investigations tend to follow existing literature when selecting materials, which can lead the field to concentrate on similar material systems and potentially become trapped in local optima. In contrast, our study employs uniform synthesis conditions—calcination at 1000 °C in ambient air—to ensure a fair comparison of the intrinsic catalytic activity of bare perovskites. This approach not only provides valuable reference data on materials that have yet to be fully optimized but also opens new opportunities for new materials discovery.

It should be accounted that MB itself degrades under Xe lamp irradiation even without a photocatalyst, as shown in Fig. 3 and Fig. S2 (ESI†). This is a critical point, since common experimental procedures involve the use of optical filters to specifically exclude the absorption band of MB itself, thereby biasing the evaluation of photocatalytic activity. A standard procedure used is irradiation with black light (which is purely UV light) to obtain quantum yields and extrapolating over photocatalytic activity under sunlight. But photocatalytic performance is known to be wavelength-dependent, and such results can be perilous to extrapolate further without further experimentation. Accordingly, in this research, photocatalytic MB degradation with and without the photocatalyst was compared under circumstances where photolysis of MB is feasible, without using cutoff filters, to ensure a fair evaluation of the photocatalytic performance.

Next, the general factors influencing photocatalytic performance are discussed based on unbiased experimental results, not influenced by previous research trends. Fig. 4 shows the relationship between material properties and performance, with multiple physical properties from the Materials Project database reduced to two dimensions using principal component analysis (PCA). In the PCA, the descriptor representing stability, "formation_energy_per_atom", and the descriptors representing the electronic structure, "vbm (valence band maximum)" and "cbm (conduction band minimum)", were chosen. It can be observed that the cbm is nearly perpendicular to the reaction rate vector, while formation_energy_per_atom is almost aligned in the opposite direction of the reaction rate vector. The perpendicular vectors suggest that these properties contribute little to performance, indicating that cbm has minimal influence on photocatalytic performance. On the other hand, the angle between vbm and the reaction rate vector is slightly greater than 90°, implying that a lower vbm might contribute to an enhanced reaction rate. Moreover, the formation_energy_per_atom, which points in the opposite direction to the reaction rate, is a descriptor related to stability—indicating that higher stability is associated with an increased reaction rate. These results suggest that descriptors based on elements or ions, which directly provide reaction sites, may capture aspects of photocatalytic performance that are not fully explained by conventional electronic structure parameters

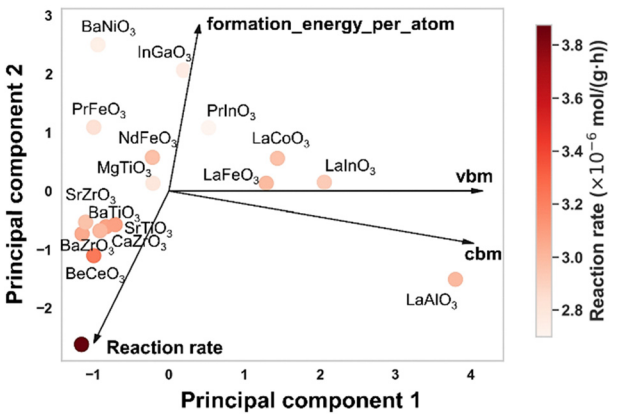

Fig. 4 Correlation between material properties and performance. It should be noted that multiple physical properties from the Materials Project database were reduced to two dimensions using PCA. The arrows represent vectors from the original dimensions displayed in 2D, with samples scattered on the 2D plane. The color of the samples indicates performance, with darker red representing higher performance.

like band edge positions. Traditionally, a higher cbm and a vbm are considered desirable for photocatalysis, as they correspond to stronger reduction and oxidation potentials, respectively. However, the present analysis indicates that these thermodynamic requirements alone may be insufficient to explain the observed activity.

Indeed, even if the cbm is high enough to thermodynamically enable a reduction reaction, sufficient photocatalytic performance cannot be achieved unless two additional kinetic conditions are met: (i) effective supply of photogenerated carriers to the surface through light absorption, exciton separation, and carrier diffusion; and (ii) fast surface reactions that overcome activation barriers.[37] This implies that photocatalytic activity is determined not only by the feasibility of the reaction (as dictated by band positions), but also by the ability to sustain carrier transport and surface reaction kinetics. In this context, the observed relevance of formation energy per atom—while unlikely to directly represent these kinetic factors—may reflect the underlying material characteristics that influence them. Consequently, this result highlights the limitations of evaluating photocatalytic activity solely based on band structure and emphasizes the need to consider kinetic descriptors that are often overlooked in conventional analysis.

4. Conclusions

This work describes an HTE approach that tackles the labor-intensive tasks associated with catalyst preparation by employing a citric acid-assisted synthesis route. One of the key strengths of this methodology is its versatility, which makes it possible to parallelly synthesize a large number of metal oxides within a short time frame. The approach is targeted not only at the parallelization of the synthesis technique but also at the screening of a wide range of perovskite compositions regarding photocatalytic performance. Such a systematic investigation, including less commonly studied perovskites, can serve for novel high-performance photocatalyst discovery, where $CaTiO_3$ stands out and shows promising performance as a photocatalytic material. Furthermore, principal component analysis based on a dataset unified in synthesis and evaluation methods suggests the limited influence of band structure on performance and highlights the greater relevance of element- or ion-based descriptors. This systematic workflow can accelerate the identification of effective photocatalysts and anticipate the necessary insights into the structure–property relationship governing photocatalytic performance.

Data availability

The data supporting this article have been included as part of the ESI.†

Conflicts of interest

There are no conflicts to declare.

Acknowledgements

This study was partly supported by Toyota Motor Corporation. We also appreciate the financial support from JSPS Kakenhi (Grant Number 24KJ1201).

References

1 S. Ali, J. Abdul Nasir, R. Nasir Dara and Z. Rehman, *Inorg. Chem. Commun.*, 2022, **145**, 110011.
2 C. Sun, J. A. Alonso and J. Bian, *Adv. Energy Mater.*, 2021, **11**, 2000459.
3 L.-P. Yuan, W.-J. Jiang, X.-L. Liu, Y.-H. He, C. He, T. Tang, J. Zhang and J.-S. Hu, *ACS Catal.*, 2020, **10**, 13227–13235.
4 C. An, Y. Zhang, H. Guo and Y. Wang, *Nanoscale Adv.*, 2019, **1**, 4644–4658.
5 J. Kim, W. Ko, J. M. Yoo, V. K. Paidi, H. Y. Jang, M. Shepit, J. Lee, H. Chang, H. S. Lee, J. Jo, B. H. Kim, S. Cho, J. van Lierop, D. Kim, K. Lee, S. Back, Y. Sung and T. Hyeon, *Adv. Mater.*, 2022, **34**, 2107868.
6 J. S. Manser, J. A. Christians and P. V. Kamat, *Chem. Rev.*, 2016, **116**, 12956–13008.
7 H. Mai, D. Chen, Y. Tachibana, H. Suzuki, R. Abe and R. A. Caruso, *Chem. Soc. Rev.*, 2021, **50**, 13692–13729.
8 K. S. Schanze, P. V. Kamat, P. Yang and J. Bisquert, *ACS Energy Lett.*, 2020, **5**, 2602–2604.
9 F. Temerov, Y. Baghdadi, E. Rattner and S. Eslava, *ACS Appl. Energy Mater.*, 2022, **5**, 14605–14637.
10 A. Kumar, A. Kumar and V. Krishnan, *ACS Catal.*, 2020, **10**, 10253–10315.
11 Z. Kalaycıoğlu, B. Özuğur Uysal, Ö. Pekcan and F. B. Erim, *ACS Omega*, 2023, **8**, 13004–13015.
12 K. Sathiyan, R. Bar-Ziv, O. Mendelson and T. Zidki, *Mater. Res. Bull.*, 2020, **126**, 110842.
13 A. Negash, S. Mohammed, H. D. Weldekirstos, A. D. Ambaye and M. Gashu, *Sci. Rep.*, 2023, **13**, 22234.
14 S. Xia, L. Zhang, G. Pan, P. Qian and Z. Ni, *Phys. Chem. Chem. Phys.*, 2015, **17**, 5345–5351.
15 C. Yang, W. Dong, G. Cui, Y. Zhao, X. Shi, X. Xia, B. Tang and W. Wang, *Sci. Rep.*, 2017, **7**, 3973.
16 J. Fito, M. Abewaa, A. Mengistu, K. Angassa, A. D. Ambaye, W. Moyo and T. Nkambule, *Sci. Rep.*, 2023, **13**, 5427.
17 J. Wang, Y. Tan, H. Yang, L. Zhan, G. Sun and L. Luo, *Sci. Rep.*, 2023, **13**, 21174.
18 Y.-Y. Lau, Y.-S. Wong, T.-T. Teng, N. Morad, M. Rafatullah and S.-A. Ong, *RSC Adv.*, 2015, **5**, 34206–34215.
19 I. Yahiaoui, F. Aissani-Benissad, K. Madi, N. Benmehdi, F. Fourcade and A. Amrane, *Ind. Eng. Chem. Res.*, 2013, **52**, 14743–14751.
20 E. H. Khader, S. A. Muslim, N. M. C. Saady, N. S. Ali, I. K. Salih, T. J. Mohammed, T. M. Albayati and S. Zendehboudi, *Desalin. Water Treat.*, 2024, **318**, 100384.
21 D. Ma, H. Yi, C. Lai, X. Liu, X. Huo, Z. An, L. Li, Y. Fu, B. Li, M. Zhang, L. Qin, S. Liu and L. Yang, *Chemosphere*, 2021, **275**, 130104.

22 P. K. Pandis, C. Kalogirou, E. Kanellou, C. Vaitsis, M. G. Savvidou, G. Sourkouni, A. A. Zorpas and C. Argirusis, *ChemEngineering*, 2022, **6**, 8.
23 V. Shinde, P. Tanwade, T. Katayama, A. Furube, B. Sathe and P. Koinkar, *Surf. Interfaces*, 2024, **46**, 104067.
24 M. A. Ashwini, S. Sagadevan, I. Fatimah, S. Paiman, S. Upadhyay, S. Garg and M. R. Johan, *J. Alloys Compd.*, 2025, **1025**, 180296.
25 C. J. Bartel, C. Sutton, B. R. Goldsmith, R. Ouyang, C. B. Musgrave, L. M. Ghiringhelli and M. Scheffler, *Sci. Adv.*, 2019, **5**, eaav0693.
26 K. Yanagiyama, K. Takimoto, S. Dinh Le, N. Nu Thanh Ton and T. Taniike, *Environ. Pollut.*, 2024, **342**, 122974.
27 P. Chammingkwan, M. Terano and T. Taniike, *ACS Comb. Sci.*, 2017, **19**, 331–342.
28 T. N. Nguyen, T. T. P. Nhat, K. Takimoto, A. Thakur, S. Nishimura, J. Ohyama, I. Miyazato, L. Takahashi, J. Fujima, K. Takahashi and T. Taniike, *ACS Catal.*, 2020, **10**, 921–932.
29 T. P. Jayakumar, S. P. Suresh Babu, T. N. Nguyen, S. D. Le, R. P. Manchan, P. Phulkerd, P. Chammingkwan and T. Taniike, *Appl. Catal., A*, 2023, **666**, 119427.
30 Y. Guo, W. Sato, K. Shoyama, H. Halim, Y. Itabashi, R. Shang and E. Nakamura, *J. Am. Chem. Soc.*, 2017, **139**, 9598–9604.
31 M. Li, M. Feng, C. Guo, S. Qiu, L. Zhang, D. Zhao, H. Guo, K. Zhang and F. Wang, *ACS Appl. Mater. Interfaces*, 2023, **15**, 16942–16952.
32 G. Dantelle, S. Beauquis, R. Le Dantec, V. Monnier, C. Galez and Y. Mugnier, *Small*, 2022, **18**, 2200992.
33 Z. Zhang, Q. Gao, Y. Liu, C. Zhou, M. Zhi, Z. Hong, F. Zhang and B. Liu, *RSC Adv.*, 2015, **5**, 84280–84283.
34 A. Jain, S. P. Ong, G. Hautier, W. Chen, W. D. Richards, S. Dacek, S. Cholia, D. Gunter, D. Skinner, G. Ceder and K. A. Persson, *APL Mater.*, 2013, **1**, 011002.
35 S. P. Ong, W. D. Richards, A. Jain, G. Hautier, M. Kocher, S. Cholia, D. Gunter, V. L. Chevrier, K. A. Persson and G. Ceder, *Comput. Mater. Sci.*, 2013, **68**, 314–319.
36 N. Vijayakumar, S. K. Venkatraman, S. Imthiaz, E. A. Drweesh, M. M. Elnagar, S. Koppala and S. Swamiappan, *Sci. Rep.*, 2023, **13**, 3615.
37 Y. Cho, K. Yanagiyama, P. Mukherjee, P. Phulkerd, K. Sathiyan, E. Sawade, T. Wada and T. Taniike, *J. Mater. Chem. A*, 2025, **13**, 16204–16211.